frontiers in Materials

ORIGINAL RESEARCH
published: 20 March 2020
doi: 10.3389/fmats.2020.00063

Core-Etched CC/SnO_2 Nanotube Arrays as High-Performance Anodes for Lithium-Ion Batteries With Ionic Liquid Electrolyte

Ao Shen[1], Ziying Zhang[1], Huizhen Zhang[2], Yangqiang Zhao[1], Pingping Xu[1], Yangyang Zhou[1] and Ying Weng[1]*

[1] School of Materials Engineering, Shanghai University of Engineering Science, Shanghai, China, [2] School of Management, University of Shanghai for Science and Technology, Shanghai, China

Despite the design of nano-structured SnO_2 anodes has attracted much attention because of its high theoretical capacity, good electron mobility, and low potential of lithium-ion intercalation, challenges remain due to their weak mechanical stability, complex processing and rapid capacity decay. The one-dimensional binder-free porous CC/SnO_2 nanotube arrays are synthesized with a well-suited core etching method to meet the needs of steady operation of flexible devices under mechanical deformation. This porous, binder-free nanostructure has large contact area with the electrolyte and excellent electron transport performance. The electrochemical measurements demonstrate that these nanotube arrays have high energy density and high-rate capability. After 500 cycles at a current density of 200 mA g^{-1}, their stable capacity remains at 595.7 mA h g^{-1}.

Keywords: carbon cloth, stannic oxide, zinc oxide, nanotube arrays, lithium-ion battery anodes

OPEN ACCESS

Edited by:
Cheng Zhong,
Tianjin University, China

Reviewed by:
Huanan Duan,
Shanghai Jiao Tong University, China
Bin Liu,
Tianjin University, China

****Correspondence:***
Ziying Zhang
zzying@sues.edu.cn

Specialty section:
This article was submitted to Energy Materials, a section of the journal Frontiers in Materials

Received: *03 February 2020*
Accepted: *28 February 2020*
Published: *20 March 2020*

Citation:
Shen A, Zhang Z, Zhang H, Zhao Y, Xu P, Zhou Y and Weng Y (2020) Core-Etched CC/SnO_2 Nanotube Arrays as High-Performance Anodes for Lithium-Ion Batteries With Ionic Liquid Electrolyte. Front. Mater. 7:63. doi: 10.3389/fmats.2020.00063

INTRODUCTION

As a green power source, lithium-ion batteries have attracted much attention because of their high energy and power density (Lee et al., 2009; Wang J. et al., 2016; Fan et al., 2019). However, the low theoretical capacity and poor cycling performance of commercial graphite anodes have hindered the further application of lithium-ion batteries (Song et al., 2017; Ding et al., 2019b). Stannic oxide (SnO_2), the typical n-type wide-bandgap semiconductor, has been considered as a potential candidate for high-performance anodes due to its high theoretical capacity (781 mA h g^{-1}), good electron mobility (240 cm^2 V^{-1} S^{-1}) and low potential of lithium ion intercalation (Tian et al., 2016; Wang M. et al., 2016). However, its volume varies greatly over the course of the cycle, causing its capacity to decay rapidly. Although SnO_2-based nano-composites have good electron transfer properties (Kim et al., 2016; Jiang et al., 2017; Lee et al., 2017; Ma et al., 2017; Guo et al., 2018), these nano-composites are mechanically unstable and usually involve complex processing processes. Therefore, it is urgent to seek an effective, economic, and scalable approach to prepare SnO_2 anode materials with satisfactory capacity and rate capability.

Recently, nanocrystals of various morphologies have been extensively used in various electrochemical energy storage devices due to their quantum size effect, large surface area, high surface activity, and remarkable electrochemical activity (Yoo et al., 2012; Ren et al., 2014; Auer et al., 2017; Qi et al., 2018; Ding et al., 2019a, 2020). Among them, one-dimensional (1D)

nanotubes have been considered as the ideal structures for anode materials of the next generation of lithium-ion batteries owing to their high surface-to-volume ratio and excellent electronic transport properties (Yoo et al., 2012; Auer et al., 2017). More importantly, the thin walls of 1D nanotubes provide a short pathway for lithium-ion diffusion and a strong resistance to structural variations (Brumbarov et al., 2015). Several recent studies have confirmed that highly ordered porous nanotube arrays grown directly on current collectors further improve the cycling performance of electrodes, since a directional porous hollow structure was expected to facilitate ionic conductivity and strain regulation (He et al., 2018; Ni et al., 2018; Tong et al., 2018). In addition, as electronics become more flexible, there is a growing demand for smaller, more flexible, higher-capacity lithium-ion batteries. Carbon cloth (CC) is one of the ideal substrates for the growth and anchorage of functional nano-arrays due to its light weight, excellent conductivity, high mechanical strength and flexibility (Liu et al., 2016; Tian et al., 2018; Zhang et al., 2019). Therefore, the direct growth of the 1D binder-free SnO_2 nanotube arrays on CC substrates was expected to be a promising strategy for obtaining high-performance anodes for the next generation rechargeable lithium-ion batteries. Although promising SnO_2@TiO_2 core/shell nanotubes on carbon cloth have been prepared by atomic layer deposition (Zhang et al., 2015), it remains a challenge to design 1D vertical SnO_2 nanotube arrays with uniform morphology on CC substrates by a facile seed-free solvothermal method.

In the present work, the 1D binder-free porous CC/SnO_2 nanotube arrays were synthesized via a well-suited core etching method. X-ray powder diffraction (XRD), field emission scanning electron microscopy (SEM) and high-resolution transmission electron microscopy (HRTEM) were used to verify the crystal structure and morphology of the obtained products. The 1D binder-free porous CC/SnO_2 nanotube arrays had a large specific surface area and good electrochemical properties due to the unique structure. After 200 cycles at a current density of 200 mA g^{-1}, their stable capacity was 724.9 mA h g^{-1}.

EXPERIMENTAL METHOD

The reagents required for this experiment are as follows: ethanol (AR, ≥99.7%), Hcl (AR, 36.0∼38.0%), ammonia (AR, 25.0∼28.0%), $C_6H_{12}N_4$ (AR, ≥99.0%), $Zn(NO_3)_2$•$6H_2O$ (AR, ≥99.0%), NaOH (AR, ≥96%), $SnCl_4$•$5H_2O$ (AR, ≥99.0%). The above reagents are all from Shanghai Chemical Reagent Co., Ltd.

Synthesis of ZnO Nanorod Cores on Carbon Cloth

ZnO nanorod arrays on carbon cloth were synthesized as the cores of the precursors by an improved wet chemical reaction method. First, the clean Saibo CC substrates were hung vertically in a 50 mL Teflon-sealed autoclave containing 40 mL of a mixed solution of 0.23 g of $Zn(NO_3)_2$•$6H_2O$, 0.12 g of hexamethylenetetramine ($C_6H_{12}N_4$) and 1.2 mL of ammonia. This Teflon-sealed autoclave was heated at 90°C for 12 h. After the autoclave was naturally cooled to room temperature, the CC substrates coated with white products were repeatedly washed with deionized water and ethanol, and then dried in a vacuum oven.

Synthesis of ZnO/SnO_2 Core-Shell Nanorod Precursors on Carbon Cloth

The prefabricated ZnO nanorod arrays were used as the templates for the growth of SnO_2 shells. In a typical procedure, 10 ml solution of 2.5 mM $SnCl_4$•$5H_2O$ and 50 mM NaOH were added into 80 mL Teflon-sealed stainless-steel autoclave containing 50 mL of a mixed solvent of ethanol/water (3:2 of v/v). After about 30 min of magnetic stirring, a piece of CC with the ZnO nanorods was immersed in the mixed solution, and maintained at 150°C for 3 h. After that, the specimens were removed from the autoclave and cleaned with distilled water and ethanol.

Synthesis of SnO_2 Nanotube Arrays on Carbon Cloth

The obtained CC/ZnO/SnO_2 core-shell nanorods were placed in a porcelain boat, and annealed in N_2 at 600°C for 30 min. The specimens immersed in 0.2 M HCl solution for 2 h to remove the ZnO cores. After that, the final products were cleaned with distillation and ethanol, and dried in air. The above reagents were selected without further purification. They were purchased from Shanghai chemical reagent co. Ltd.

Structure and Morphology Characterization

The crystallographic structure of the obtained products was examined by XRD (Panalytical X' Pert, Holland) with Cu-Ka radiation ($\lambda = 1.5418$ Å). The structure and morphology of the obtained products were characterized by SEM (JSM-7000F, Japan) and HRTEM (TitanX 60–300, USA). The X-Ray photoelectron spectroscopy (XPS) measurements were performed by using Perkin-Elmer model PHI 5600 XPS System with monochromated aluminum anode as the X-ray source. The mass loading of active materials was calculated by measuring the weight difference between the prepared electrodes and CC substrates using an FA1004 electronic balance. The specific surface area of the specimens was calculated by Brunauer-Emmett-Teller (BET) method based on the measurement of nitrogen adsorption-desorption isotherm on a Micrometics Tristar 3,000 system.

Electrochemical Measurements

Electrochemical measurements were carried out in coin-type cells (CR2032), which were assembled in an argon-filled glovebox by using a piece of binder-free porous CC/SnO_2 nanotube arrays as the anode material and a lithium-metal circular foil as the counter and reference electrodes. The electrolyte was 1 M solution of $LiPF_6$ dissolved in ethylene carbonate and Dimethyl carbonate (DMC) (1:1 of v/v). The galvanostatical charge and discharge tests of the cells were executed on the multi-channel battery tester (Neware-CT3008). Cyclic voltammetry (CV) were recorded on a PARSTAT 4000 electrochemical workstation at a scan rate of 0.2 mV s^{-1} in the range of 3.0–0.005 V vs. Li/Li^+.

Electrochemical impedance spectroscopy (EIS) was carried out in the frequency range of 100 kHz to 0.01 Hz with an ac perturbation voltage of 5 mV.

RESULTS AND DISCUSSION

Synthesis and Characterization

The growth process of 1D binder-free porous CC/SnO_2 nanotube arrays is schematically illustrated in **Figure 1A**. First, the ZnO nanorod cores were grown on CC substrates by wet chemical reaction. Secondly, a SnO_2 shell was coated on the surface of the ZnO nanorods by a simple hydrothermal process. Finally, the ZnO nanorod cores were removed from the annealed CC/ZnO/SnO_2 core-shell precursors by HCl solution etching.

The obtained CC/ZnO and CC/SnO_2 products were identified by XRD measurements. As shown in **Figure 1B**, the broad peaks of both products at about 26 and 43° were caused by the contribution of the CC substrates. CC/ZnO products crystallized into standard hexagonal ZnO (JCPDS No. 36–1451) (Tang et al., 2018), and their lattice parameters were a = b = 3.250 Å and C = 5.207 Å. The peaks of the final CC/SnO_2 products were determined to be the pure tetragonal rutile SnO_2 (JCPDS no. 41–1445) (Dong et al., 2017), and no additional diffraction peaks from ZnO were detectable. The calculated lattice parameters of SnO_2 were a = b = 4.74 Å and C = 3.19 Å, which agrees well with the experimental values (Wang et al., 2012).

XPS measurements were executed to analyze the specific elemental composition and chemical bonding state of the final CC/SnO_2 product surface. **Figure 2A** illustrates that the XPS survey spectrum of the CC/SnO_2 products only contained O, C, and Sn elements, and no other impurities were found. The XPS spectrum of the C1s core-level (**Figure 2B**) was decomposed into three peaks of 284.5, 285.2, and 289.1 eV, respectively. The highest peak at 284.5 eV was derived from non-oxygenated carbon. The other two weak peaks were mainly contributed by a degree of oxidation produced during the chemical bath and annealing process. The peak of the O 1s spectrum (**Figure 2C**) consisted of three components. The main peak lied at 530.19 eV was derived from Sn–O–Sn (lattice O^{2-}) of stannic oxide. Whereas, the peaks of 531.3 and 532.3 eV represented C=O and C–O, respectively. This is consistent with the results obtained from the C1s spectrum. The binding energies of Sn $3d_{5/2}$ and Sn $3d_{3/2}$ (**Figure 2D**) were ∼486.2 and ∼494.7 eV, respectively. These characteristic bands confirm the complete oxidation of Sn on the surface to Sn^{4+}. This is consistent with the above XRD test results.

The morphologies and the microstructure of the as-prepared precursors were further characterized by SEM and TEM. **Figures 3a,b** show the SEM images of CC/ZnO nanorod arrays at different magnification. It can be seen that the 1D rod-like ZnO grew vertically and homogeneously on the surfaces of CC substrates, with an average diameter of ∼150 nm. The uniform brightness and smooth surface confirm that the microstructure of ZnO nanorods was dense with no noticeable pores (**Figure 3c**). The HRTEM images shown in **Figures 3d,e** reveal that the ZnO nanorods have a lattice spacing of 0.247 nm, corresponding to the (101) planes of wurtzite-type ZnO (Ramasamy and Lee, 2011). **Figure 3f** shows the SEM images of the intermediate products obtained by coating SnO_2 shell on the surface of CC/ZnO nanorod arrays. Although the obtained CC/ZnO/SnO_2 core-shell nanorod arrays were still arranged in an orderly manner, they had a larger mean diameter and a rougher surface than the bare CC/ZnO nanorod arrays.

Figures 4a,b show the morphology of the final products at different magnification. It can be seen that the ZnO nanorod cores of the intermediate products were dissolved and removed after etching in HCl solution. The binder-free CC/SnO_2 nanotube arrays had an open end and no obvious structural defects. **Figures 4c–e** shows a typical TEM image of the SnO_2 nanotubes disassembled from a CC substrate by ultrasonic vibration.

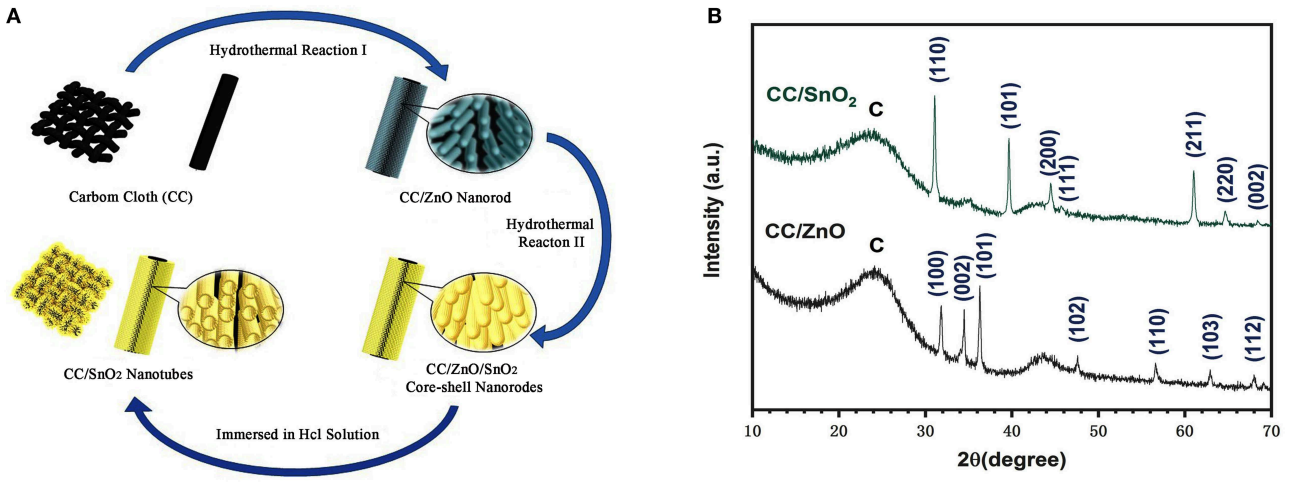

FIGURE 1 | (A) Schematic illustration of the synthesized procedures of 1D binder-free porous CC/SnO_2 nanotube arrays. **(B)** XRD pattern of 1D binder-free porous CC/SnO_2 nanotube arrays.

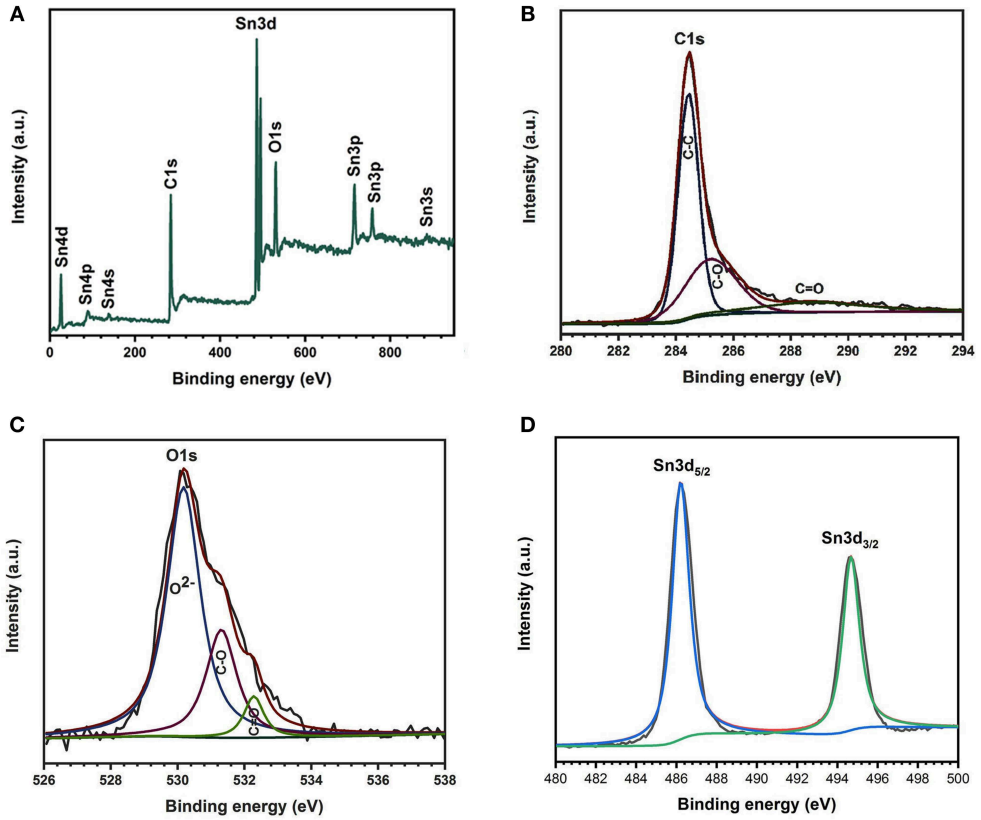

FIGURE 2 | XPS spectra of 1D binder-free porous CC/SnO_2 nanotube arrays. **(A)** Survey spectra. **(B)** C1s core-level spectra, **(C)** O1s core-level spectra. **(D)** Sn3d core-level spectra.

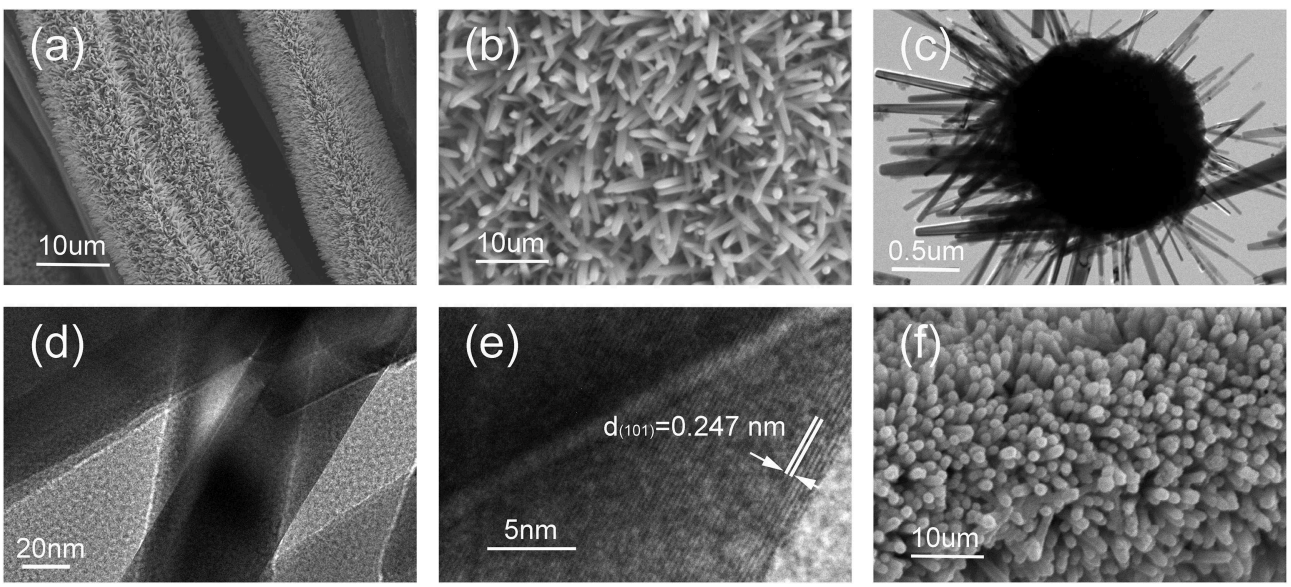

FIGURE 3 | SEM and TEM images of the prepared precursors. **(a,b)** SEM images of CC/ZnO nanorod arrays at different magnifications. **(c)** TEM images of CC/ZnO nanorod arrays. **(d,e)** HRTEM images of CC/ZnO nanorod arrays. **(f)** SEM images of CC/ZnO/SnO_2 core-shell nanorod arrays.

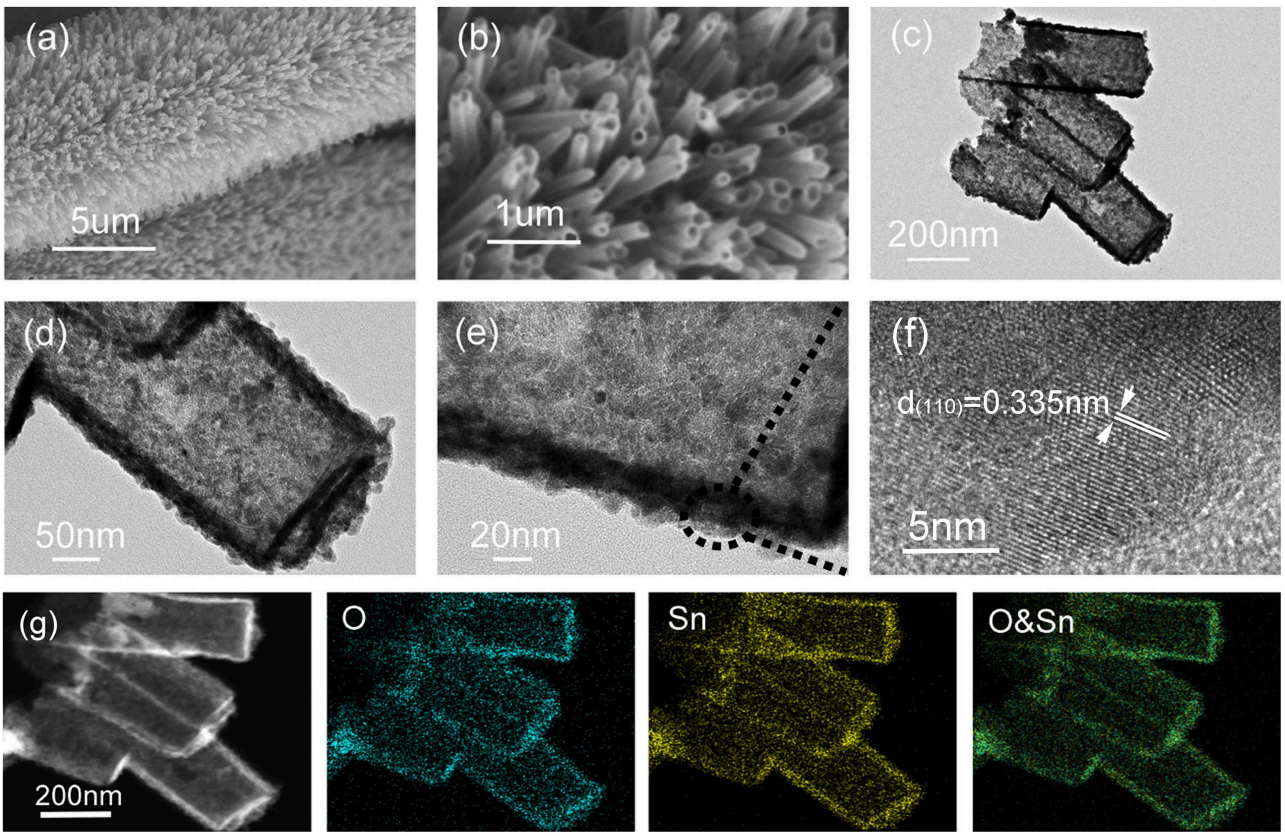

FIGURE 4 | SEM and TEM images of CC/SnO_2 nanotube arrays. **(a,b)** SEM images of CC/SnO_2 nanotube arrays at different magnifications. **(c)** TEM images of SnO_2 nanotubes. **(d–f)** HRTEM images of SnO_2 nanotubes. **(g)** TEM elemental mapping images of SnO_2 nanotubes.

The diameter of SnO_2 nanotubes was about 100–200 nm and the thickness of their shells was about 10–20 nm. The weight difference between the final products and the pure CC substrates indicated that the mass loading of the binder-free CC/SnO_2 nanotube arrays was ∼8.3 mg cm^{-2}. Further HRTEM analysis indicates that the SnO_2 nanotube arrays inherited the rough surface of the intermediate CC/ZnO/SnO_2 core-shell nanorod arrays. Their rough surface provides a rich adsorption interface for absorbing lithium-ions. The walls of the SnO_2 nanotube arrays consisted of nanoparticles with diameters of 2–5 nm. **Figure 4f** displays the corresponding lattice fringes with an interlayer spacing of 0.335 nm, which was in agreement with the (110) planes of SnO_2 (Ramasamy and Lee, 2010). The EDX mapping shows that Sn and O elements in the SnO_2 nanotube arrays were evenly distributed (**Figure 4g**). Similar to the XPS results, no other elements except Sn and O were detected in the EDS of SnO_2 nanotube arrays (**Figure S1**).

The specific surface area and porosity of the 1D binder-free CC/SnO_2 nanotube arrays were further determined by the nitrogen sorption analysis. The nitrogen adsorption-desorption isotherm and pore size distribution of the 1D binder-free CC/SnO_2 nanotube arrays are depicted in **Figure 5A**. Type IV isotherm validated the mesoporous structure of the obtained nanotube arrays. N_2 Isotherm Tabular Report indicates that their specific surface area was 168.4 m^2 g^{-1}, which was higher than that of SnO_2 nanoparticles (about 30 m^2 g^{-1}). Pore size was mainly distributed in the range of 1–12 nm (**Figure 5B**). Such mesoporous CC/SnO_2 nanotube arrays facilitated the insertion-extraction of lithium-ions.

Electrochemical Properties

The electrochemical properties of the binder-free porous CC/SnO_2 nanotube arrays were tested using lithium foil as the counter electrode. **Figure 6A** illustrates the first three CV curves of these nanotube arrays at a scanning rate of 0.2 mVs^{-1}. In the first cathodic step, the reduction peak in the range of 0–0.4 V corresponded to the alloying reaction of Sn and Li, while the peak at ∼0.95 V was mainly ascribed to the formation of the solid-state electrolyte interface (SEI) film and the reduction reaction of SnO_2 (Zhou et al., 2012). The anodic peak at ∼0.4 V was contributed to the dealloying process of Li_xSn alloy. The electrochemical reaction mechanism between Li and SnO_2 electrode is as follows

$$SnO_2 + 4Li^+ + 4e^- \Rightarrow Sn + 2Li_2O \quad (1)$$

$$xLi^+ + xe^- + Sn \Leftrightarrow Li_xSn \quad (2)$$

In the following cycles, no significant changes were found except the disappearance of the mapping peak of SEI film. The

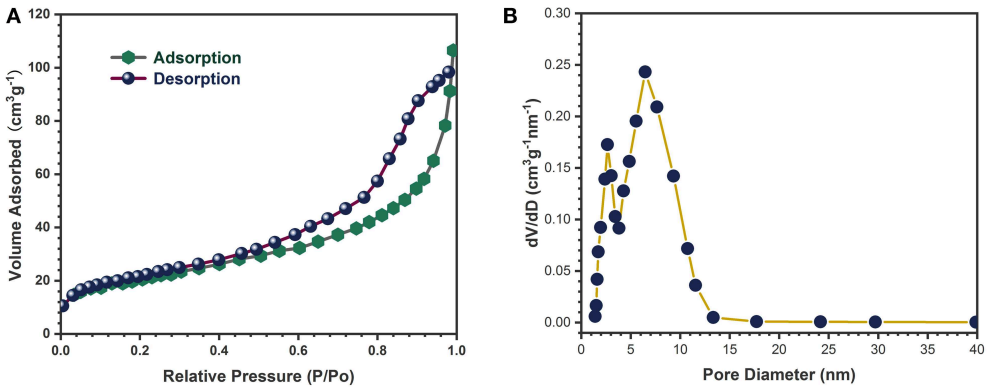

FIGURE 5 | (A) Nitrogen adsorption/desorption isotherms and **(B)** Pore size distribution of CC/SnO_2 nanotube arrays.

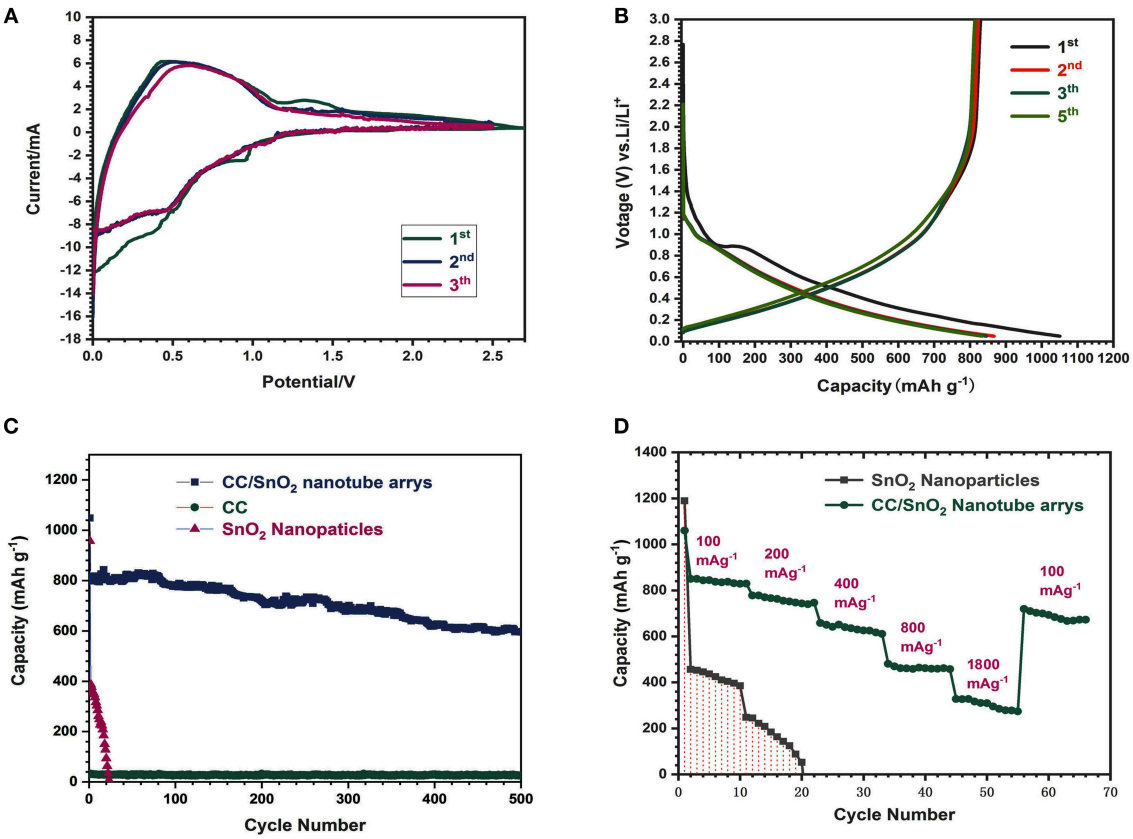

FIGURE 6 | (A) CV curves of CC/SnO_2 nanotube arrays. **(B)** Charge-discharge voltage profiles of CC/SnO_2 nanotube arrays at a constant current rate of 200 mAg^{-1}. **(C)** Cycling performances of CC/SnO_2 nanotube arrays, SnO_2 nanoparticles, and pure CC at a constant current rate of 200 mA g^{-1}. **(D)** Rate performances of CC/SnO_2 nanotube arrays as well as SnO_2 nanoparticles.

second and third CV curves overlapped well and decreased slightly compared to the first CV curve, indicating that the electrochemical reaction had good reversibility (Zhou et al., 2012; Qi et al., 2018).

Figure 6B depicts the charge-discharge profiles of the binder-free porous CC/SnO_2 nanotube arrays at the current density of 200 mA g^{-1}. An evident plateau was observed at ~0.95 V in the first discharge curve. This discharge plateau is due to the formation of the SEI film (Zhou et al., 2012). The initial discharge and charge capacities of the binder-free porous CC/SnO_2 nanotube arrays were ~1149.6 and ~831.8 mA h g^{-1}, respectively, corresponding to a lower irreversible capacity loss

(∼12.4 %) caused by the incomplete conversion reactions and the formation of a SEI layer. The charge-discharge profiles of the second, third, fourth and fifth curves almost overlapped with each other, indicating a stable electrochemical performance. This is consistent with the CV testing results. **Figure 6C** shows the cycling performance of the electrodes made from the binder-free porous CC/SnO_2 nanotube arrays and the commercial SnO_2 nanoparticles, respectively. After 500 cycles, the binder-free porous CC/SnO_2 nanotube arrays maintained a capacity of 595.7 mA h g^{-1}, while the capacity of the commercial SnO_2 nanoparticles decayed to almost zero after 23 cycles. Here, it should be noted that the initial capacity of the nanotube arrays is slightly higher than their theoretical capacity due to the contribution of CC substrate. The SEM image of the 500-cycled electrodes demonstrated that the binder-free porous CC/SnO_2 nanotube arrays (**Figure S2**) were tightly attached to the CC surface and remained intact after 500 cycles. The above-mentioned electrodes were cycled at various current densities (100–1,800 mA g^{-1}) to further verify their rate capability. Compared with nanoparticles, the binder-free porous CC/SnO_2 nanotube arrays exhibited an excellent rate performance (**Figure 6D**). Even at the high current densities of 1,800 mA g^{-1}, the stable capacity of 380 mA h g^{-1} could be maintained. In contrast, the SnO_2 nanoparticle electrodes with a mass loading of 3.06 mg cm^{-2} failed completely before the 200 mA g^{-1} current cycle. According to the previous literature (Gogotsi and Simon, 2011; Xia et al., 2016; Qi et al., 2018), the large reversible capacity is contributed mainly by the high mass loading and large specific surface area, while the high rate capability and remarkable cycling stability are mainly due to the binder-free porous 1D hollow architecture and their thin walls.

The electrochemical impedance spectroscopy (EIS) measurements were further performed to explore trends in electrochemical activity of the binder-free porous CC/SnO_2 nanotube arrays. The Nyquist plots of the binder-free porous CC/SnO_2 nanotube arrays and the commercial SnO_2 nanoparticles are displayed in **Figure 7**. In the Nyquist plots of the first and 50th cycled binder-free porous CC/SnO_2 nanotube array electrodes, two semicircles were found in the high to middle frequency range, and a straight sloping line in the low frequency range. According to the Randles equivalent circuit inserted into **Figure 7A**, the semicircle in the high frequency region corresponds to the resistance (R_{SEI}) and capacitance (C_{SEI}) of the SEI layer and the semicircle with a large radius in the middle frequency region represents the double-layer capacitance (C_{DI}) and the charge transfer process (R_{CT}), while the sloping line in the low frequency region reflects the Warburg impedance (Zw) related to the solid-state diffusion of lithium-ions (Qi et al., 2018). In contrast, the resistance (R_{SEI}) and capacitance (C_{SEI}) of the SEI layer contributed less to the Nyquist plots of commercial SnO_2 nanoparticles owing to their small specific surface area and low electron transfer (**Figure 7B**). The corresponding Randles equivalent circuit was also inserted in **Figure 7B**. The binder-free porous CC/SnO_2 nanotube arrays had a lower charge transfer resistance than the commercial SnO_2 nanoparticles, with only a slight increase after 50 cycles. Their charge transfer resistance was 6.65 and 8.84 Ω, respectively, for the first and 50th cycled electrodes. This indicates that the binder-free porous CC/SnO_2 nanotube array electrodes exhibited an excellent conductivity due to the faster rate of charge transfer (lithium-ion migration) on the 1D hollow electrodes. This leads to better cycle stability and rate capability.

CONCLUSIONS

In summary, the 1D binder-free porous CC/SnO_2 nanotube arrays were successfully synthesized by using a suitable core etching method. The 1D binder-free porous SnO_2 nanotube arrays grown vertically and homogeneously on the conductive CC substrates have not only a large specific surface area, but also excellent electronic transport performance. This unique structure endowed the 1D binder-free porous CC/SnO_2 nanotube arrays with a large reversible capacity, remarkable cycling stability, high rate capability and excellent conductivity. At a current density of 200 mA g^{-1}, the 1D binder-free porous

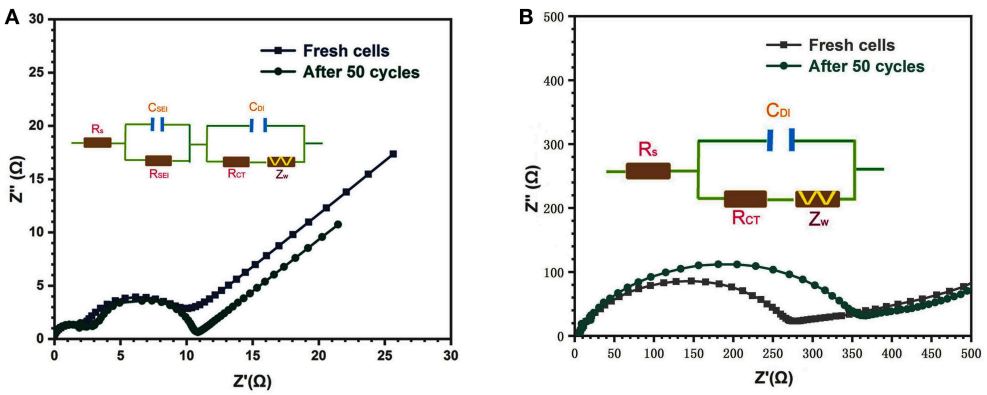

FIGURE 7 | Impedance analysis of CC/SnO_2 nanotube arrays **(A)** and SnO_2 nanoparticles **(B)**.

CC/SnO_2 nanotube arrays still maintained a specific capacity of 595.7 mA h g^{-1} after 500 cycles. Their stable capacity remained at 380 mA h g^{-1} even at high current densities of 1,800 mA g^{-1}.

DATA AVAILABILITY STATEMENT

All datasets generated and analyzed for this study are included in the article.

AUTHOR CONTRIBUTIONS

AS conducted the experiments. ZZ is the supervisor of this research work. AS, HZ, and ZZ helped with writing. YZhao, YZhou, PX, and YW performed the characterization and data analysis. All authors involved the analysis of experimental data and manuscript preparation.

FUNDING

This work was supported by National Natural Science Foundation of China (Grant No. 71401106), Shanghai Natural Science Foundation (Grant No. 14ZR1418700), and Shanghai University of Engineering Science Innovation Fund (Grant No. 18KY0504).

ACKNOWLEDGMENTS

The authors would like to thank Minjie Yan for his help with SEM/EDX analysis.

SUPPLEMENTARY MATERIAL

The Supplementary Material for this article can be found online at: https://www.frontiersin.org/articles/10.3389/fmats.2020.00063/full#supplementary-material

REFERENCES

Auer, A., Portenkirchner, E., Götsch, T., Valero-Vidal, C., Penner, S., and Kunze-Liebhäuser, J. (2017). Preferentially oriented TiO_2 nanotubes as anode material for Li-Ion batteries: insight into Li-Ion storage and lithiation kinetics. *ACS Appl. Mater. Interfaces* 9, 36828–36836. doi: 10.1021/acsami.7b11388

Brumbarov, J., Vivek, J. P., Leonardi, S., Valero-Vidal, C., Portenkirchner, E., and Kunze-Liebhäuser, J. (2015). Oxygen deficient, carbon coated self-organized TiO_2 nanotubes as anode material for Li-ion intercalation. *J. Mater. Chem. A* 3, 16469–16477. doi: 10.1039/C5TA03621F

Ding, J., Liu, Z., Liu, X., Liu, B., Liu, J., Deng, Y., et al. (2020). Tunable periodically ordered mesoporosity in palladium membranes enables exceptional enhancement of intrinsic electrocatalytic activity for formic acid oxidation. *Angew. Chem. Int. Ed*. doi: 10.1002/anie.201914649

Ding, J., Liu, Z., Liu, X., Liu, J., Deng, Y., Han, X., et al. (2019a). Mesoporous decoration of freestanding palladium nanotube arrays boosts the electrocatalysis capabilities toward formic acid and formate oxidation. *Adv. Energy Mater*. 9:1900955. doi: 10.1002/aenm.201900955

Ding, J., Zhang, H., Zhou, H., Feng, J., Zheng, X., Zhong, C., et al. (2019b). Sulfur-Grafted hollow carbon spheres for potassium-Ion battery anodes. *Adv. Mater*. 31:1900429. doi: 10.1002/adma.201900429

Dong, W., Xu, J., Wang, C., Lu, Y., Liu, X., Wang, X., et al. (2017). A robust and conductive black Tin Oxide nanostructure makes efficient Lithium-Ion batteries possible. *Adv. Mater*. 29:1700136. doi: 10.1002/adma.201700136

Fan, X., Liu, X., Hu, W., Zhong, C., and Lu, J. (2019). Advances in the development of power supplies for the internet of everything. *InfoMat*. 1, 130–139. doi: 10.1002/inf2.12016

Gogotsi, Y., and Simon, P. (2011). True performance metrics in electrochemical energy storage. *Science* 334, 917–918. doi: 10.1126/science.1213003

Guo, W., Wang, Y., Li, Q., Wang, D., Zhang, F., Yang, Y., et al. (2018). SnO_2@C@VO_2 composite hollow nanospheres as an anode material for Lithium-Ion batteries. *ACS Appl. Mater. Interfaces* 10, 14993–15000. doi: 10.1021/acsami.7b19448

He, J., Chen, Y., and Manthiram, A. (2018). Vertical Co_9S_8 hollow nanowall arrays grown on a Celgard separator as a multifunctional polysulfide barrier for high-performance Li–S batteries. *Energy Environ. Sci*. 11, 2560–2568. doi: 10.1039/C8EE00893K

Jiang, B., He, Y., Li, B., Zhao, S., Wang, S., He, Y. B., et al. (2017). Rücktitelbild: polymer-templated formation of polydopamine-coated SnO_2 nanocrystals: anodes for cyclable Lithium-Ion batteries. *Angew. Chem*. 129, 1958–1958. doi: 10.1002/ange.201700375

Kim, C., Jung, J. W., Yoon, K., Youn, R. D. Y., Park, S., and Kim, I. D. (2016). A high-capacity and long-cycle-life Lithium-Ion battery anode architecture: silver nanoparticle-decorated SnO_2/NiO nanotubes. *ACS Nano*. 10, 11317–11326. doi: 10.1021/acsnano.6b06512

Lee, K., Shin, S., Degen, T., Lee, W., and Yoon, Y. S. (2017). *In situ* analysis of SnO_2/Fe_2O_3/RGO to unravel the structural collapse mechanism and enhanced electrical conductivity for lithium-ion batteries. *Nano Energy* 32, 397–407. doi: 10.1016/j.nanoen.2016.12.058

Lee, Y. J., Yi, H., Kim, W. J., Kang, K., Yun, D. S., Strano, M. S., et al. (2009). Fabricating genetically engineered high-power lithium-ion batteries using multiple virus genes. *Science* 324, 1051–1055. doi: 10.1126/science.1171541

Liu, J., Guan, C., Zhou, C., Fan, Z., Ke, Q., Zhang, G., et al. (2016). A flexible quasi-solid-state nickel-zinc battery with high energy and power densities based on 3D electrode design. *Adv. Mater* 28, 8732–8739. doi: 10.1002/adma.201603038

Ma, T., Yu, X., Li, H., Zhang, W., Cheng, X., Zhu, W., et al. (2017). High volumetric capacity of hollow structured SnO_2@Si nanospheres for Lithium-Ion batteries. *Nano Lett*. 17, 3959–3964. doi: 10.1021/acs.nanolett.7b01674

Ni, J., Fu, S., Yuan, Y., Ma, L., Jiang, Y., Li, L., et al. (2018). Boosting sodium storage in TiO_2 nanotube arrays through surface phosphorylation. *Adv. Mater*. 30:1704337. doi: 10.1002/adma.201704337

Qi, X., Zhang, H., Zhang, Z., Bian, Y., Shen, A., Xu, P., et al. (2018). Subunits controlled synthesis of three-dimensional hierarchical flower-like α-Fe_2O_3 hollow spheres as high-performance anodes for lithium ion batteries. *Appl. Surf. Sci*. 452, 174–180. doi: 10.1016/j.apsusc.2018.04.253

Ramasamy, E., and Lee, J. (2010). Ordered mesoporous SnO_2-based photoanodes for high-performance dye-sensitized solar cells. *J. Phys. Chem. C* 114, 22032–22037. doi: 10.1021/jp1074797

Ramasamy, E., and Lee, J. (2011). Ordered mesoporous Zn-doped SnO_2 synthesized by exotemplating for efficient dye-sensitized solar cells. *Energy Environ. Sci*. 4, 2529–2536. doi: 10.1039/c1ee01123e

Ren, H., Yu, R., Wang, J., Jin, Q., Yang, M., Mao, D., et al. (2014). Multishelled TiO_2 hollow microspheres as anodes with superior reversible capacity for Lithium Ion batteries. *Nano Lett*. 14, 6679–6684. doi: 10.1021/nl503378a

Song, W., Brugge, R., Theodorou, I. G., Lim, A. L., Yang, Y., Zhao, T., et al. (2017). Enhancing distorted metal-organic framework-derived ZnO as anode material for lithium storage by the addition of Ag_2S quantum dots. *ACS Appl. Mater. Interfaces* 9, 37823–37831. doi: 10.1021/acsami.7b12661

Tang, W., Wang, X., Xie, D., Xia, X., Gu, C., and Tu, J. (2018). Hollow metallic 1T MoS_2 arrays grown on carbon cloth: a freestanding electrode for sodium ion batteries. *J. Mater. Chem. A* 6, 18318–18324. doi: 10.1039/C8TA06905K

Tian, R., Duan, H., Guo, Y., Li, H., and Liu, H. (2018). High-coulombic-efficiency Carbon/Li clusters composite anode without precycling or prelithiation. *Small* 14:1802226. doi: 10.1002/smll.201802226

Tian, R., Zhang, Y., Chen, Z., Duan, H., Xu, B., Guo, Y., et al. (2016). The effect of annealing on a 3D SnO_2/graphene foam as an advanced lithium-ion battery anode. *Sci. Rep*. 6:19195. doi: 10.1038/srep19195

Tong, Z., Liu, S., Li, X., Mai, L., Zhao, J., and Li, Y. (2018). Achieving rapid Li-ion insertion kinetics in TiO_2 mesoporous nanotube arrays for

bifunctional high-rate energy storage smart windows. *Nanoscale* 10, 3254–3261. doi: 10.1039/C7NR07703C

Wang, J., Tang, H., Zhang, L., Ren, H., Yu, R., Jin, Q., et al. (2016). Multi-shelled metal oxides prepared via an anion-adsorption mechanism for lithium-ion batteries. *Nat. Energy* 1:16050. doi: 10.1038/nenergy.2016.50

Wang, M., Yang, H., Zhou, X., Shi, W., Zhou, Z., and Cheng, P. (2016). Rational design of SnO_2@C nanocomposites for lithium ion batteries by utilizing adsorption properties of MOFs. *Chem. Commun.* 52, 717–720. doi: 10.1039/C5CC07983G

Wang, X., Cao, X., Bourgeois, L., Guan, H., Chen, S., Zhong, Y., et al. (2012). N-Doped Graphene-SnO_2 sandwich paper for high-performance Lithium-Ion batteries. *Adv. Funct. Mater.* 22, 2682–2690. doi: 10.1002/adfm.201103110

Xia, L., Wang, S., Liu, G., Ding, L., Li, D., Wang, H., et al. (2016). Flexible SnO_2/N-Doped carbon nanofiber films as integrated electrodes for Lithium-Ion batteries with superior rate capacity and long cycle life. *Small* 12, 853–859. doi: 10.1002/smll.201503315

Yoo, J. K., Kim, J., Jung, Y. S., and Kang, K. (2012). Scalable fabrication of silicon nanotubes and their application to energy storage. *Adv. Mater.* 24, 5452–5456. doi: 10.1002/adma.201201601

Zhang, H., Ren, W., and Cheng, C. (2015). Three-dimensional SnO_2@TiO_2 double-shell nanotubes on carbon cloth as a flexible anode for lithium-ion batteries. *Nanotechnology* 26:274002. doi: 10.1088/0957-4484/26/27/274002

Zhang, Z., Xu, P., Zhang, H., Shen, A., and Zhao, Y. (2019). Flexible three-dimensional titanium-dioxide-based hollow nanoflower arrays for advanced Lithium-Ion battery anodes. *ACS Appl. Energy Mater.* 2, 5744–5752. doi: 10.1021/acsaem.9b00869

Zhou, X., Yin, Y. X., Wan, L. J., and Guo, Y. G. (2012). A robust composite of SnO_2 hollow nanospheres enwrapped by graphene as a high-capacity anode material for lithium-ion batteries. *J. Mater. Chem.* 22, 17456–17459. doi: 10.1039/c2jm32984k

Conflict of Interest: The authors declare that the research was conducted in the absence of any commercial or financial relationships that could be construed as a potential conflict of interest.